# Fixed-bed column adsorption studies of methylene blue dye from an aqueous solution using silicon nitride adsorbent synthesized from sand and coffee husk wastes

**Ndung'u Samuel Ng'ang'a[1*], Nthiga Esther Wanja[2], Wanjau Ruth Nduta[1], Gichumbi Joel Mwangi[3]**

[1]*Department of Chemistry, Kenyatta University, P.O Box 43844-00100, Nairobi, Kenya*
[2]*Department of Chemistry, Dedan Kimathi University of Technology, P.O Box 657-10100, Nyeri, Kenya*
[3]*Department of Physical Sciences, Chuka University, P.O Box 109-60400, Chuka, Kenya*

Corresponding author: Ndung'u Samuel Ng'ang'a; E-mail: samuelndungu530@gmail.com; Tel number: +254710302380

## ABSTRACT

To address the challenge of increased demand for clean water globally, there is a need to treat the available wastewater. Textile dyes are carcinogenic and their discharge to the environment has been reported to degrade the esthetic properties of water bodies. It is imperative to assess textile dye levels in wastewater as well as decontamination to ascertain its safety. Conventional purification processes suffer from limitations in terms of efficiency, cost effectiveness and environmental effect. Attention has recently shifted to adsorption as an economical technique for textile dyes removal using low-cost adsorbents. The current study utilizes Silicon Nitride ($Si_3N_4$) as a novel adsorbent in evaluating its adsorptive ability for Methylene blue dyes from an aqueous solution. The adsorbent was prepared using extracted silica from sand and coffee husk biochar in an ammonia environment. The sand, extracted silica, raw and biochar samples and silicon nitride composites were characterized using X-Ray Fluorescence (XRF), Fourier Transform Infrared (FT-IR), X-Ray Diffractometer (XRD), Scanning Electron Microscope (SEM), Energy Dispersive X-Ray (EDX) and Thermogravimetric Analyzer (TGA). The results showed that the raw sand contain quartz, calcite, microcline and clinochlore. The results for the extracted silica showed a highly amorphous silica containing hydroxyl (-OH) and siloxane (Si-O-Si) functional groups. The alkali fusion process increased the silica content to > 92 % from 83 % with oxide impurities reduced to < 1 %. The characterization of biochar samples showed a highly amorphous, porous carbon structure with aromatic carbon bonds (C=C) and a negligible ash content. The characterization of $Si_3N_4$ powder showed thermally stable, porous and highly amorphous material with $\alpha$-$Si_3N_4$ and $\beta$- $Si_3N_4$ phases. The FT-IR results functional groups of silicon-nitrogen (Si-N), silanol (Si-OH) and silicon-nitrogen-silicon (Si-N-Si) which were hydroxylated in an aqueous media to give silazane ($Si_2=NH_2^+$) and silanolate ($Si\text{-}O^-$) adsorbent sites for methylene blue (MB) dyes removal. A column capacity (47.01 mg/g) was reported at optimal values of 4 mL/min, 7 cm and 50 mg/L. Column dynamic modeling analysis revealed that Thomas and Yoon-Nelson models best fitted the breakthrough curves than Adam-Bohart model. The column performance using spiked water samples Athi showed that $Si_3N_4$ adsorbent had a lower efficacy than in a model solution with the maximum column adsorption capacity of 38.92 ± 0.04 mg/g. The results revealed the potential of $Si_3N_4$ adsorbent for decontamination of MB dyes from wastewater.

**KEYWORDS:** Methylene blue (MB) dye, fixed-bed adsorption, breakthrough curves

## 1. INTRODUCTION

Access to safe water is vital for sustainable life (Ndung'u *et al.,* 2021). The main challenge encountered daily is increased water consumption due to rapid population growth, urbanization and continued industrial advancements (Bulgariu *et al.,* 2019). The various anthropogenic activities have increased loads of contaminants to the water supply system compromising water quality. Among the contaminants are dyes with their extensive use in many applications such as in pulp and paper, tanneries, textiles, packed food industries, pharmaceuticals, petroleum, plastics, electroplating, paint and cosmetics industries (Saha *et al.,* 2012). Their presence in water even at their low concentrations, influences the visibility, appearance and quality of water, which is esthetically nasty (Bennani *et al.,* 2015). These dyes are synthetic and of complex aromatic structures which make them more stable and non-biodegradable therefore hardly eliminated from wastewater (Patel, 2018). In addition, dyes are also loaded with heavy metals such as lead, zinc, chromium, copper and cobalt in trace amounts produced during the dyeing process making them toxic, carcinogenic and mutagenic (Ngulube *et al.,* 2017).

Methylene blue ($C_{16}H_{18}ClN_3S$) is an industrial thiazine cationic dye that contain chromophoric and auxochromic groups. The chromophoric groups imparts the dye colour by undergoing strong π-π and n-*π* electronic transitions in the UV-visible area (Ngulube *et al.,* 2017). The auxochromes intensifies the colour of the chromophore by altering the overall energy of the electron system (Aroke *et al.,* 2020). The dye dissociate easily in aqueous media since the auxochromic groups are weakened by the structural stability imparted by the extensive chromophore conjugation and the high degree of aromaticity (Mcyotto *et al.,* 2021). The dye has hetero-polyaromatic structure which presents a strong inhibitive function for biological degradation (Liu *et al.,* 2019). The dye has been reported to cause harmful effects such as increased jaundice, vomiting, heart rate, cyanosis, tissue necrosis, quadriplegia, dermatitis, problems in liver, respiratory tract, brain, kidney and central nervous system (Patel *et al.,* 2019). It is therefore imperative for industries to look for sustainable, cost effective, innovative and greener treatment methods essential in mitigating these impacts.

These colored wastewaters are usually treated using various conventional techniques that often entail physical or chemical processes (Parmar and Shukla, 2019). However, they are reported to be pricey, less effective and adaptable to a range of dyes in wastewater (Muliwa *et al.,* 2016). Many scientists and environmentalists have gained research interests on the adsorption technology due to its simplicity in operation, environmentally friendly and highly efficient (Jain *et al.,* 2020). Also, most research report on the dye wastewater treatment via batch processes limiting the usability of the adsorbents in an industrial scale containing high load of textile dye wastewater (Mohammad *et al.,* 2016). There is therefore a pressing need to investigate the potential of a $Si_3N_4$ adsorbent derived from sand and coffee husk biochar in fixed-bed column treatment of textile dye wastewater. The adsorbent surface is reported to undergo hydroxylation in an aqueous media yielding acidic silanol (Si-OH) and silazane ($Si_2$=NH) groups which then upon hydroxylation make the surface charged (Shi *et al.,* 2014; Ndung'u *et al.,* 2024). The current study, a continuation of work reported by Ndung'u *et al.,* 2024 and Ndung'u *et al.,* 2023 b investigates the potential of a $Si_3N_4$ adsorbent derived from extracted silica from sand, biochar from coffee husk wastes for sorption of MB dye from an aqueous media.

## 2. MATERIAL AND METHODS

### 2.1 Chemicals and reagents

Analar (> 99.5% purity) grade chemicals and reagents were used in this study. Sodium hydroxide (NaOH), Hydrochloric acid (HCl), Ammonium solution ($NH_4OH$) and Nitric (V) acid ($HNO_3$) were all sourced from Kobian limited (outlet of Sigma Aldrich), Nairobi, Kenya. Distilled water obtained from Kenyatta University chemistry laboratory was used throughout the study.

### 2.2 Apparatus and instrumentation

The glassware was soaked in 10 % $HNO_3$ overnight and then scrubbed using a scotch brush, washed using hot water containing detergent, soaked in aqua regia (1 % $HNO_3$ / 3 % HCl) overnight, rinsed thoroughly with distilled water and air-dried. The instruments and equipment used were Thermogravimetric Analyzer (TGA-50 SHIMADZU), X-Ray Diffractometer (Rigaku MiniFlex II; Tokyo in Japan), Field Emission Scanning electron microscope (FEI ESEM, Vega3 Tescan LMH), Pulveriser rock grinding machine (Retsch RS 200), Automated X-Ray Fluorescence Spectrometer (Bruker S1 Titan 600, Tracer 5/ CTX), Fourier Transform Infrared Spectrophotometer (IR Tracer-100, Japan), Grinding mill (Retsch SR 200), Distiller (WSB 14), Magnetic stirrer with hot plate (WH240-HT), Drying oven (WTC binder FD53), Thermostat-controlled muffle furnace (MC5-12 Biobase) and Analytical weighing balance (ATX224 Shimadzu).

### 2.3 Sample collection

Sand samples were collected from the Bamburi beach (-3.98822'S, 39.73678'E) in Mombasa, Kenya, transported to Kenyatta University laboratories, pre-treated and stored in airtight container awaiting subsequent experiments. The coffee husk wastes were randomly collected in Othaya Constituency (-0.551751'S, 36.944703'E) in Nyeri County, cleaned using distilled water, chopped and oven-dried at 105 $^{o}$C for 24 hours to remove moisture. The final material was then ground into a fine powder.

### 2.4 Silica extraction

The silica was extracted using a method described by Ndung'u *et al.* (2023 a). A 100.000 g of the sand powder was soaked in 6 N HCl solution in a glass beaker for 12 hours. The mixture was then filtrated, the residue washed with distilled water until there is no yellowish color and then dried at 105 °C to a constant weight. A 400 mL of 10 N NaOH solution was then added to the sand residue and heated at 150 $^{o}$C while stirring for 4 hours. The filtrate (sodium silicate) was separated from the unreacted sand residues using Whatmann filter paper No. 1 and 6 N HCl solution slowly added to form a white gel (pH 7). The reaction mixture was left overnight at room temperature, filtered and rinsed with distilled water. The gel was then dried at 105 °C to a constant weight to obtain amorphous silica.

### 2.5 Biochar preparation

A 20 g of the biomass powder was first dried in an oven at 105 $^{o}$C for 24 hours and a constant weight recorded. The pyrolysis was performed in a thermostat-controlled muffle furnace at a frequency of 50 Hz, 10 °C/min (heat rate), voltage of 220 V and power output of 3.0 kW. The powder was placed in a ceramic crucible and pyrolyzed at 300 $^{o}$C for 5 hours (Fachini *et al.*, 2021). The biochar sample was allowed to cool, ground and weighed. The percentage yield was determined as the ratio of mass of biochar to mass of dried sample expressed as a percentage (Equation 1).

$$\text{Yield (\%)} = \frac{\text{Mass of biochar}}{\text{Mass of the dried sample}} \times 100 \qquad (1)$$

Part of the obtained biochar was acid leached using 3 M HCl acid for 3 hours to remove any inorganic ash components (Alvarez *et al.*, 2016). The biochar material was then washed with distilled water to eliminate excess acid, oven-dried at 105 $^{o}$C to a constant weight and stored in airtight bottles labelled CHB. The biochar sample was characterized using FT-IR, XRD, SEM and EDX.

The proximate analysis of the other part of the biochar samples was performed according to the gravimetric method of the ASTM (D1762-84) standard methods.

### 2.6 Silicon nitride ($Si_3N_4$) adsorbent preparation

The preparation of silicon nitride adsorbent was carried out first by carbothermal reduction followed by nitridation process described by Maroufi *et al.* (2018) and Abdulhameed *et al.* (2018) with slight modifications. The process was performed using a digestion bomb locally made at Kenyatta University mechanical engineering laboratories, school of engineering. The bomb was made of a stainless steel (SS-316) whose cylindrical body was 105 mm in total length, 38 mm in external diameter, 23.5 mm in internal diameter. The top lid had a total length of 39 mm and thread length of 23.5×1.5×22 mm. The biochar powder was mixed with the extracted silica in the ratio of 3 to 2 for two hours and then placed in a digestion bomb. The bomb was tightly closed and placed in a thermostat-controlled muffle furnace and heated at 300 $^{o}$C for 12 hours and the final product allowed to cool. Approximately 200 mL of $NH_4OH$ solution (28 % v/v) was then added, bomb tightly closed and heating continued at 300 $^{o}$C for another 12 hours. The final product was then allowed to cool, ground and stored in an airtight container awaiting characterization.

### 2.7 MB dye solution

A stock MB dye solution (1000 ppm) was prepared by dissolving 1.000 g the dye solute in $C_2H_3O_2Na$ buffer solution to 1 L. Then, serial dilutions were done to obtain working solutions.

### 2.8 Fixed-bed studies

A glass column of 25 cm in length and 1 cm internal diameter was packed with a glass wool at both ends and then equipped with a peristaltic pump (Longer-BT100) for fixed-bed column experiments at 298 K. The $Si_3N_4$ adsorbent was then loaded in the column and wetted with distilled water to eliminate any trapped air in the adsorbent particles. The dye effluent was collected at pre-defined time intervals (10-300 minutes). The effect of bed height (3-7 cm), volumetric flow rate (4-6 mL/min) and influent concentration (50 mg/L-90 mg/L) on uptake capacity was investigated. The resultant solution was analyzed for the amount of dyes adsorbed using UV-Visible Spectrophotometer (Specord 200, Analytik Jena) at $\lambda_{max}$ of 600 nm.

### 2.9 Column performance using environmental water samples

The environmental water samples were collected from river Athi, Mavoko, Machakos county. They were taken randomly from seven different sampling points along the shores of the river. Five samples of 1 L were taken from each sampling point and 5 mL of concentrated $HNO_3$ acid added to each sample, bottles sealed and samples were transported to Kenyatta University laboratories. A 100 mL of the water sample from each of the sampling point was placed in a beaker. The analysis of the amount of dye solution found in environmental water samples was determined. Then, known concentration (50 mg/L) of MB dye standards were spiked into the water sample. The spiked water sample was loaded in the fixed-bed column containing $Si_3N_4$ adsorbent at an optimal bed height. The water sample (3 L) was pumped through the fixed-bed column in a down flow mode at optimal flow rate. The samples were collected at specified time intervals of 10 minutes and the concentration of dye in the effluent was analyzed using UV-Vis spectrophotometer. The retained dyes in the adsorbent were stripped with 0.1 M HCl or 0.1 M NaOH solutions.

### 2.10 Data evaluation

The amount adsorbed in the column is calculated by using Equation 2.

$$Q_{total} = \frac{Q}{1000}\int_{t=0}^{t_{total}} C_{ads}\,dt \qquad (2)$$

Where Q: flow rate (mL/min), $t_{total}$: total flow time (min), $C_{ads}$: difference between initial and final concentration.

The column capacity ($Q_{exp}$) is calculated using Equation 3.

$$Q_{exp} = \frac{Q_{total}}{m} \qquad (3)$$

Where m: adsorbent mass (g).

### 2.11 Breakthrough curve modelling

The column models (Yoon-Nelson, Adams-Bohart and Thomas) are used to fit the column time data. Thomas model assumes a second-order reaction kinetics and the Langmuir isotherm adsorption (Iheanacho *et al.*, 2021). Its linearized form is given by Equation 4.

$$\ln\left(\frac{C_o}{C_t} - 1\right) = k_{TH}Q_o\frac{m}{Q} - k_{TH}C_o t \qquad (4)$$

Where $C_o$ and $C_t$ are influent and effluent concentrations (mg/L**),** $k_{Th}$. rate constant (ml/mg/min) and $Q_o$: column capacity (mg/g).

The Yoon-Nelson model assumes that the dye adsorbed is half the initial amount of dye entering the fixed-bed within a period of time ($t_{1/2}$) (Nica *et al.*, 2020). Its linearized expression is given by Equation 5.

$$\ln\left(\frac{C_t}{C_o - C_t}\right) = k_{YN}t - \tau k_{YN} \qquad (5)$$

Where $k_{YN}$ ($min^{-1}$): rate constant, and τ (min): time required for 50 % adsorbate breakthrough (i.e. $C_t/C_0 \approx 0.5$).

The Adams-Bohart model assumes that equilibrium is not-instantaneous and rate of sorption is proportional to the fraction of sorption capacity (Ndung'u *et al.*, 2022). The linearized form is given by Equation 6.

$$\ln\left(\frac{C_t}{C_o}\right) = K_{AB}C_o t - \frac{K_{AB}N_o Z}{U_o} \tag{6}$$

where t: flow time (min), $K_{AB}$: rate constant (L/mg/min), $N_o$: maximum saturation concentration (mg/L), Z: bed height (cm), and $U_o$: superficial velocity (cm/min).

## 3. RESULTS AND DISCUSSION

### 3.1 Characterization of raw sand and extracted silica

### 3.1.1 XRD analysis

The XRD results for the raw sand (before and after acid treatment) and the extracted silica (ES) are shown by Figure 1.

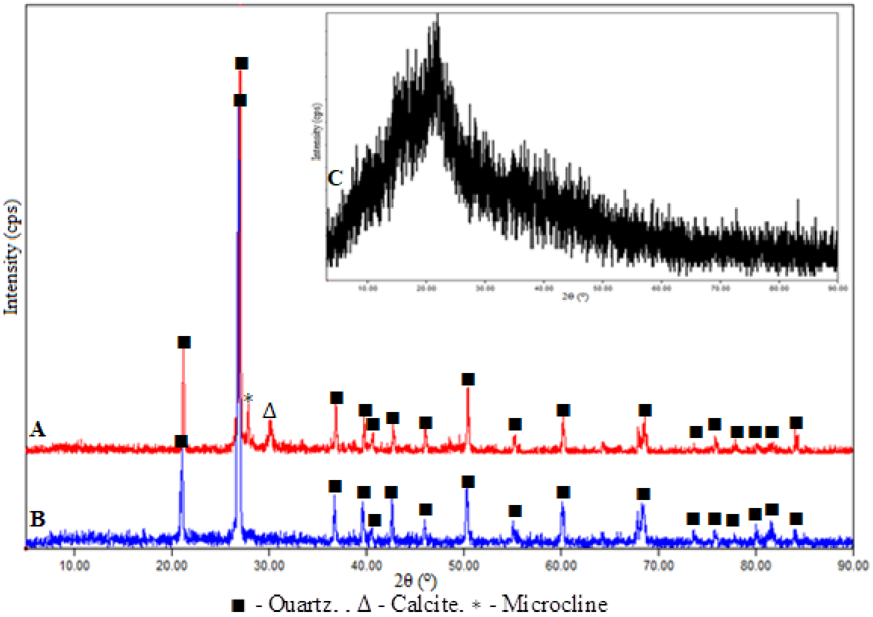

**Figure 1:** The XRD pattern of raw sand (A), acid-treated sand (B) and the extracted silica (C)

The results (diffractogram A) show that quartz ($SiO_2$) (JCPDS-ICDD file No. 46-1045), calcite ($CaCO_3$) (JCPDS-ICDD file No. 47-1743) and microcline (K (Al, Fe) $Si_3O_8$) (JCPDS-ICDD file No. 19-0932) are the main components of sand. A minor mineral phase of clinochlore ($(Mg, Fe)_6(Si, Al)_4O_{10}(OH)_8)$) (JCPDS-ICDD file No. 07-0078), although its crystal planes does not appear in the XRD patterns, is also suggested by the Match! software version 3.14 Build 238. A characteristic peak at 2θ 26.4 ° indicates the high crystallinity of the quartz phase (El-Sawy *et al.*, 2021). This is in agreement with the findings reported by Munasir *et al.* (2015) during their research study on the synthesis of $SiO_2$ nanopowders containing quartz and cristobalite phases from silica sands.

The peaks at 28.3 ° and 29.99 ° for microcline and calcite minerals disappeared in the acid treated sand (B). This implied that the purification process eliminated the major impurities in the sand to negligible amounts (Bousbih *et al.*, 2020). From the results in diffractogram C, a broad characteristic peak at 20.71° with the absence of any other intense peaks indicated the presence of a highly pure amorphous silica (JCPDS-ICDD file No. 001-0424). Also, the crystallite size was 31.84 nm showing that the silica was in nanoscale size (Ndung'u *et al.*, 2023).

### 3.1.2 XRF analysis

The chemical composition of the raw sand (BBS), acid treated sand (ABBS) and the extracted silica (ES) was determined by XRF. The results are presented in Table 1.

**Table 1:** Mean percentage of chemical composition of BBS, ABBS and ES

| **Sample** | **Oxide (%)** | | | | | |
|---|---|---|---|---|---|---|
| | $SiO_2$ | CaO | $K_2O$ | $Al_2O_3$ | $Fe_2O_3$ | MgO |
| BBS | 83.46 ± 0.39 | 6.48 ± 1.01 | 3.54 ± 0.14 | 2.62 ± 0.34 | 2.56 ± 0.07 | 0.99 ± 0.11 |
| ABBS | 88.14 ± 0.06 | 3.04 ± 0.03 | 0.12 ± 0.04 | 1.59 ± 0.22 | 1.95 ± 0.05 | 0.19 ± 0.04 |
| ES | 92.72 ± 0.63 | 0.25 ± 0.04 | nd | 0.09 ± 0.01 | 0.99 ± 0.09 | nd |

*nd – not detected

From the results in Table 1, the silica content of the raw sand was 83.46 ± 0.39 % with a low concentration of CaO (6.48 ± 1.01 %), $K_2O$ (3.54 ± 0.14 %), $Al_2O_3$ (2.62 ± 0.34 %), $Fe_2O_3$ (2.56 ± 0.07 %) and MgO (0.99 ± 0.11 %). This showed that silica was the main component of the raw sand. The calcium oxide content could due to the presence of calcite ($CaCO_3$) mineral in the sand samples (Hachem *et al.*, 2023). The iron, magnesium, potassium and aluminium oxide contents could indicate the presence of minerals such as microcline (K (Al, Fe) $Si_3O_8$) and clinochlore ($(Mg, Fe)_6(Si, Al)_4O_{10}(OH)_8$) in the silica matrix. This is in agreement with the XRD results.

The acid treatment of the sand samples increased the silica content to 88.14 ± 0.06 % while the amount of the other oxide components reduced. The purification process resulted to a mass decrease of the sand by 8.32 %. The yellowish-white colour was observed in the sand samples after acid treatment. This could be due to the residue iron contents in the acid-treated sand (Alyosef *et al.*, 2014). The results showed that the sand obtained were highly pure with minimal mass loss (< 10 %). The results are in agreement with those reported by Meftah *et al.* (2023) during their studies on extraction and physicochemical characterization of highly-pure amorphous silica nanoparticles from locally available dunes sand.

The analysis of the extracted silica shows that the silica content of 92.72 ± 0.63 % which corroborates the extraction of highly pure silica. The other oxide components were to negligible amounts. This showed that alkali fusion increased not only the silica content but also eliminated the remaining impurities that had remained in the sand after acid leaching (Munasir *et al.*, 2013).

### 3.1.3 FT-IR analysis

The raw sand, acid treated sand and extracted silica were characterized by FT-IR at a mid IR range of 4000 - 400 $cm^{-1}$. The results are presented in Figure 2.

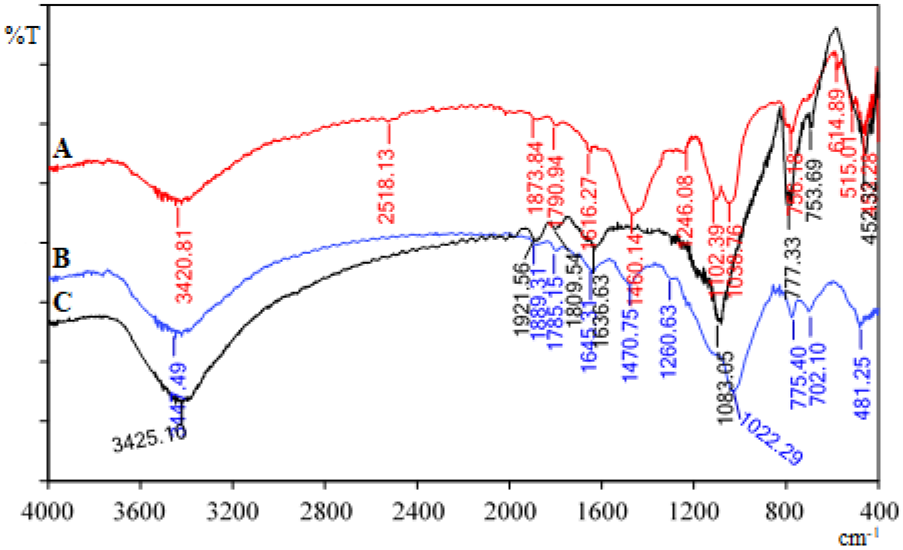

**Figure 2:** The FT-IR spectra of raw sand (A), acid-treated sand (B) and the extracted silica (C)

The results for the raw sand (A) shows a broak peak at 3420.81 cm$^{-1}$ which was attributed to -OH stretch mode of water molecules in the sand (Zouaouid and Gheriani, 2018). This was confirmed by its flexion vibration at 1616.27 cm$^{-1}$. The peaks at 2518.13 cm$^{-1}$ and 1460.14 cm$^{-1}$ could be due to asymmetrical and symmetrical stretch vibrations of $CO_3^{2-}$ groups (Meftah and Mahboub, 2019). This was confirmed by a peak at 1790.94 cm$^{-1}$ attributed to the C=O stretch mode (Hachem *et al.*, 2023). This suggested the presence of calcite ($CaCO_3$) in the sand samples. The characteristic peaks at 1038.76 cm$^{-1}$ and 756.18 cm$^{-1}$ were ascribed to the Si-O-Si asymmetric and symmetric stretch vibrations (Yang *et al.*, 2023). Absorption bands observed at 614.89 cm$^{-1}$ corresponded to Si-O-Fe and Si-O-Mg stretch vibrations (Beddiaf *et al.*, 2015). Also, at 515.01 cm$^{-1}$ was a band for asymmetric Si-O-Al stretch vibrations (Abdelhak *et al.*, 2014). This could be due clinochlore and microcline mineral components in the silica matrix. The peaks at 453.28 cm$^{-1}$ were associated with Si-O-Si bend mode (Yue *et al.*, 2018). The results confirm XRD and XRF results.

The FTIR spectrum for acid treated sand (B) showed peaks at 3447.49 cm$^{-1}$, 1645.31 cm$^{-1}$, 1022.29 cm$^{-1}$, 775.40 cm$^{-1}$ and 481.25 cm$^{-1}$ indicative of quartz in the sand. All the peaks showed shifting to higher or lower values. This could be influenced by reduction of impurities contained in the sample (Panwar *et al.*, 2015). The peak intensity for 1470.75 cm$^{-1}$ and 1785.15 cm$^{-1}$ was lower than that of the raw sand. Also, peaks at 2518.13 cm$^{-1}$ disappeared after acid treatment. This showed that acid treating the raw sand decreased the calcite mineral contents in the sand samples. The peaks at 515.01 cm$^{-1}$ and 605.66 cm$^{-1}$ also disappeared after the acid treatment. The lost absorption bands showed elimination of the calcite, clinochlore and microcline impurities to lower amounts.

The FTIR spectrum of the extracted silica (C) showed peaks at 3425.10 cm$^{-1}$ and 1636.63 cm$^{-1}$ assigned to hydroxyl ($OH^-$) in silanol groups and/or adsorbed water molecules (Ndung'u *et al.*, 2023). Additionally, absorption bands at 1083.05 cm$^{-1}$, 777.33 cm$^{-1}$ and 452.32 cm$^{-1}$ correspond to the asymmetric, symmetric and bend vibration of Si-O-Si bonds respectively (Arunmetha *et al.*, 2015).

## 3.2 Biochar characterization

### 3.2.1 Proximate analysis

The percentage yield and proximate analysis of CHB was determined and results are tabulated in Table 2.

**Table 2:** Proximate analysis of the CHB

| Analysis wt (%) | (Mean ± S.D) |
|---|---|
| Yield | 25.11 ± 0.12 |
| Moisture | 7.45 ± 0.00 |
| Volatile matter | 74.80 ± 5.93 |
| Ash | 1.02 ± 0.27 |
| Fixed carbon | 16.73 ± 2.01 |

The results in Table 2 showed that a high volatile matter of 74.80 ± 5.93 % was released during the pyrolytic treatment of the raw biomass. This showed that all the volatiles trapped within the biomass matrix was eliminated forming biochar with a high carbon content (Bushra and Remya, 2020). The biochar had a carbon and ash content of 16.73 ± 2.01 % and 1.02 ± 0.27 respectively. The results indicated that the biochar obtained has a high carbon content and negligible ash content.

### 3.2.2 FT-IR analysis

The FT-IR analysis for both waste coffee husks and the char obtained by pyrolysis are shown in Figure 3.

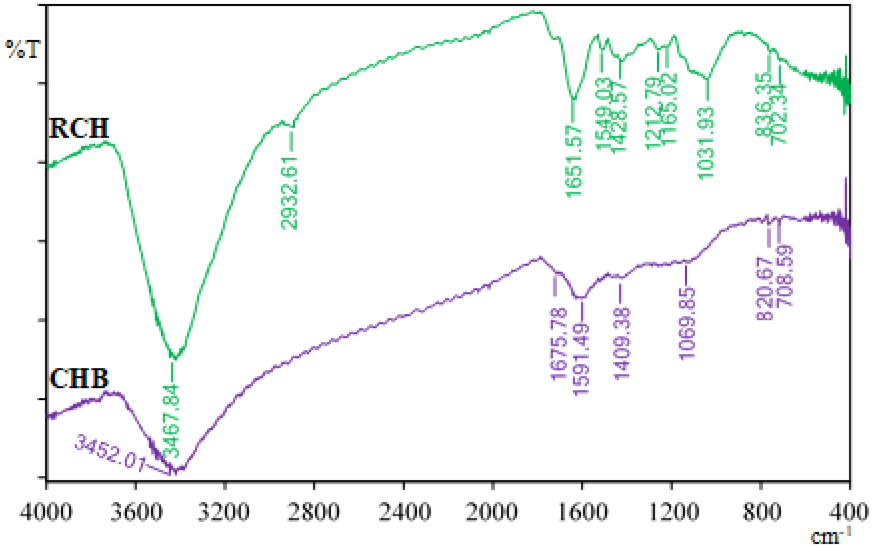

**Figure 3:** FT-IR spectra of raw coffee husk (RCH) and coffee husk biochar (CHB)

The results in FT-IR spectrum of the raw biomass showed a strong band at 3467.84 cm$^{-1}$ which indicated bonded hydroxyl (-OH) groups. (Krishna Murthy *et al.*, 2020). The peak at 2932.61 cm$^{-1}$ was attributed to $CH_2$ stretch mode in aliphatic groups (Alghamdi and El Mannoubi, 2021). The absorption peak at 1651.57 cm$^{-1}$ correspond to carbonyl (C=O) groups stretch in carboxylic acid and its derivatives (Ndung'u *et al.*, 2021). The peak at 1549.03 cm$^{-1}$ could be due to carbon-carbon

(C=C) stretching vibrations of aromatic hydrocarbons (Mansuri *et al.*, 2018). This was confirmed by its bend mode at 836.35 $cm^{-1}$. The bands observed in 1212.79 $cm^{-1}$ and 1031.93 $cm^{-1}$ could be ascribed to C-O stretch vibrations of carboxylic acid derivatives and alcoholic groups (Nthiga *et al.*, 2021). The same peak at 1031.93 $cm^{-1}$ together with a peak at 702.34 $cm^{-1}$ could also be due to the stretching vibrations of Si-O-Si functional groups (Huljana *et al.*, 2021). The results confirmed the presence of silica in the raw biomass materials.

The methyl peak for the biochar FT-IR spectrum disappeared indicating the absence of the aliphatic carbon (Chen *et al.*, 2023). The spectrum showed a distinguished peak at 1591.49 $cm^{-1}$ for C=C groups confirming the presence of aromatic carbon content (Kabayo *et al.*, 2019). The FT-IR spectrum didn't show any other major peaks which showed that there was complete pyrolysis of coffee husk wastes.

### 3.2.3 XRD analysis

The biochar sample was prepared by pyrolytic treatment of the raw coffee husks followed by acid leaching and XRD results are shown in Figure 4.

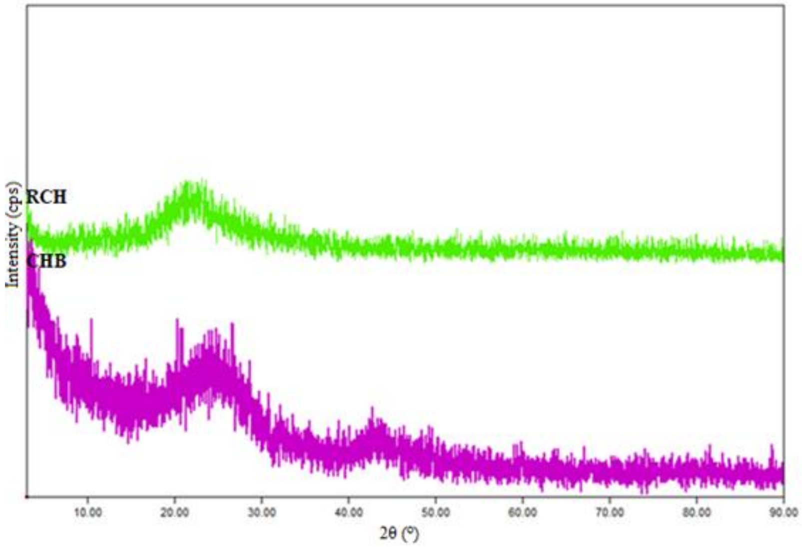

**Figure 4:** The XRD pattern of raw coffee husk (RCH) and coffee husk biochar (CHB)

The results in Figure 4 showed broad diffraction peaks at 21.97° showing that the raw biomass contains lignin, hemicellulose, pectin and cellulosic materials which are highly amorphous (Mu *et al.*, 2018). This corresponded to a diffraction peak for amorphous cellulose (JCPDS-ICDD file No. 03-0226). The same peak provides information on amorphous silica in the raw coffee husk biomass and its biochar (JCPDS-ICDD file No. 001-0424). The XRD diffractograms for CHB show diffraction patterns at $2\theta = 24.14°$ and $2\theta = 44.73°$ which correspond to the highly amorphous and diffuse graphite peaks (JCPDS-ICDD file No. 41-1487). This characterized a predominantly amorphous carbon structure (Jagdale *et al.*, 2019). There was no evidence of any inorganic phases in the XRD pattern showing that the prepared biochar sample had negligible ash content (Lawrinenko and Laird, 2015).

### 3.2.4 SEM analysis

The surface morphology of RCH and CHB was performed by Scanning Electron Microscope (SEM) at an accelerating voltage of 20.0 kV. The SEM micrographs obtained are presented in Figure 5.

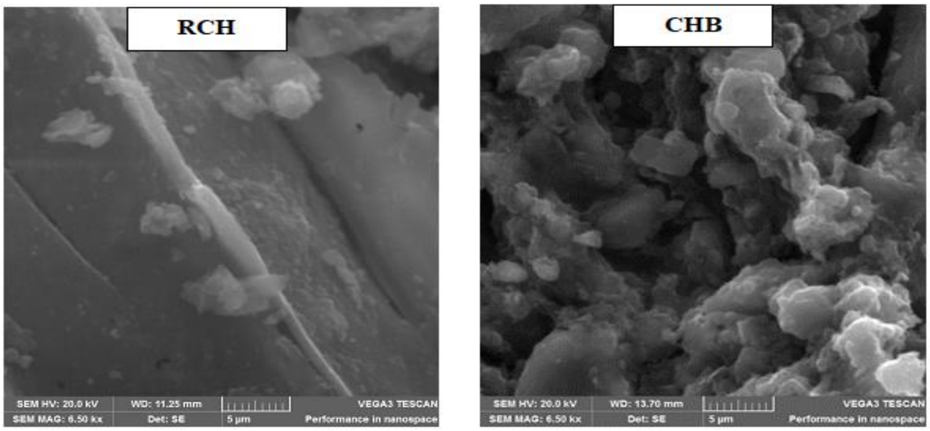

**Figure 5:** SEM micrograph for RCH and CHB

From the results in Figure 5, the SEM micrographs showed changes in the biochar surface texture and morphology before and after pyrolysis. The raw biomass surface structure was rigid, regular and less porous. After pyrolysis, the biochar surface became rugged and more porous. This is due to the rapid decomposition of volatile compounds during pyrolysis making the surface rougher and irregular (Sahoo *et al.*, 2020).

### 3.2.5 EDX analysis

The EDX spectra of raw coffee husk (RCH) and coffee husk biochar (CHB) are shown in Figure 6.

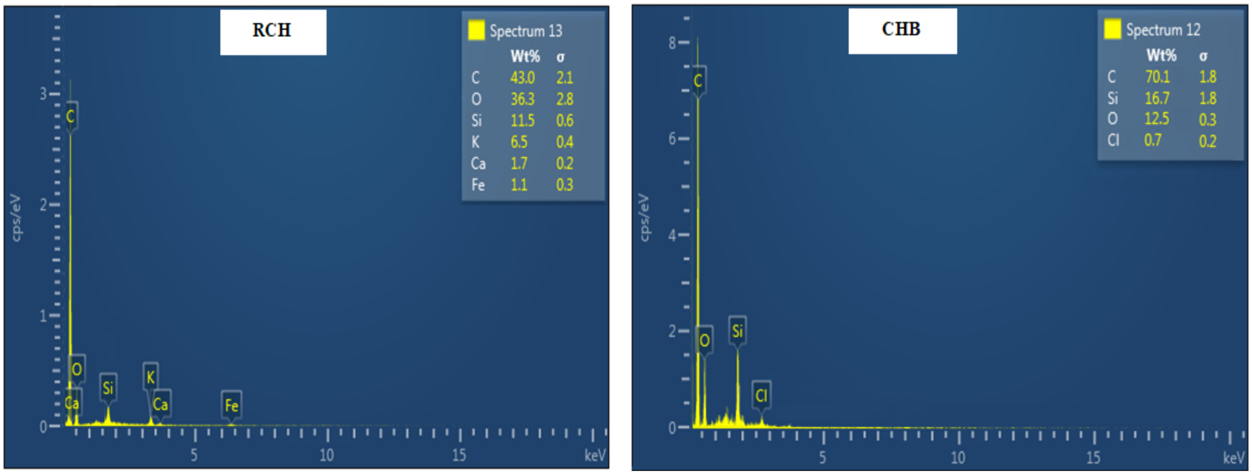

**Figure 6:** EDX spectra of RCH and CHB

From the results in Figure 6, the composition of RCH was 43.0 % (C), 36.3 % (O), 11.5 % (Si), 6.5 % (K), 1.7 % (Ca) and 1.1 % (Fe). The EDX spectrum showed the presence of carbon (C) and oxygen (O) as the main components of raw coffee husk. The elemental oxygen could also be as attributed to surface oxides of silica and metallic elements. The elemental composition of CHB was 70.1 % (C), 16.7 % (Si), 12.5 % (O) and 0.7 % (Cl). The final biochar showed a higher carbon and silica content with negligible ash contents comparatively to the raw biomass material. This showed that pyrolytic treatment followed by acid washing of the biochars not only decreased the inorganic ash contents from the biochar (Chang *et al.*, 2019) but also increased the carbon content. The chloride contents were detected in the final biochar material. This could be due to residue acid after the materials were washed with distilled water (Abdulhameed *et al.*, 2018).

### 3.3 Characterization of silicon nitride ($Si_3N_4$) adsorbent

#### 3.3.1 FT-IR analysis

The FT-IR analysis of $Si_3N_4$ adsorbent were recorded at a range of 4000 - 400 $cm^{-1}$ and the results are presented in Figure 7.

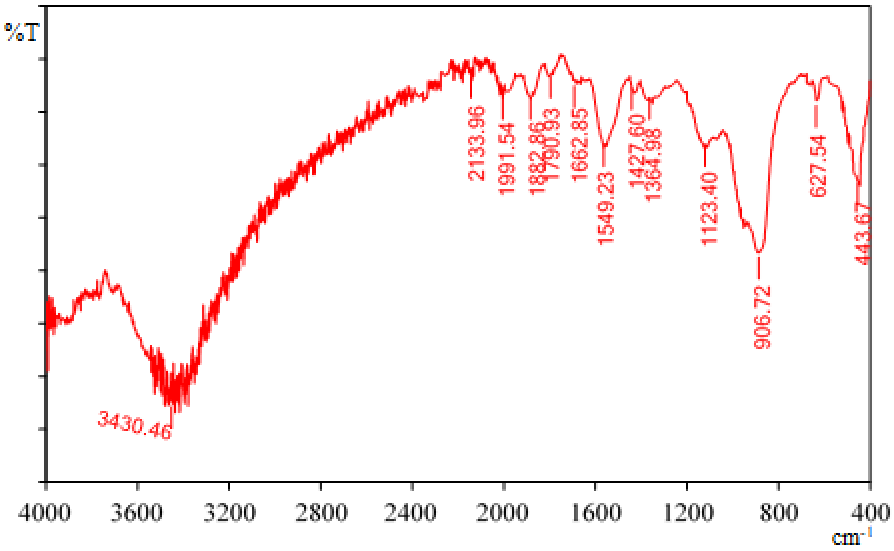

**Figure 7:** FT-IR spectrum of $Si_3N_4$ adsorbent

The FT-IR spectrum of the $Si_3N_4$ adsorbent showed a broad peak at 3430.46 $cm^{-1}$ corresponding to stretching vibrations of N-H and -OH of silanol (Si-OH) groups (Kobayashi, 2016). The peak at 1662.85 $cm^{-1}$ could be due to $OH^-$ bending vibration of silanol functional groups (Ramdani *et al.*, 2014). The absorbance peaks at 1549.23 $cm^{-1}$are indicative of the N-H bending modes (Shi *et al.*, 2014). The peaks at 1123.40 $cm^{-1}$ could be ascribed to Si-O-C stretching vibration (Liang *et al.*, 2020). The bands at 906.72 $cm^{-1}$ was ascribed to the Si-N-Si stretching vibrations (Jhansirani *et al.*, 2016). The peak at 627.54 $cm^{-1}$ may correspond to a Si-Si stretching mode (Cui *et al.*, 2015). The absorption peak observed at 443.67 $cm^{-1}$ was for Si-N stretching vibration in α-silicon nitride phase (Huang *et al.*, 2013).

#### 3.3.2 XRD analysis

The XRD analysis of $Si_3N_4$ adsorbent was performed at an applied current of 40 mA, accelerating voltage of 45 kV and the step size of 0.02. The diffractogram obtained is presented in Figure 8.

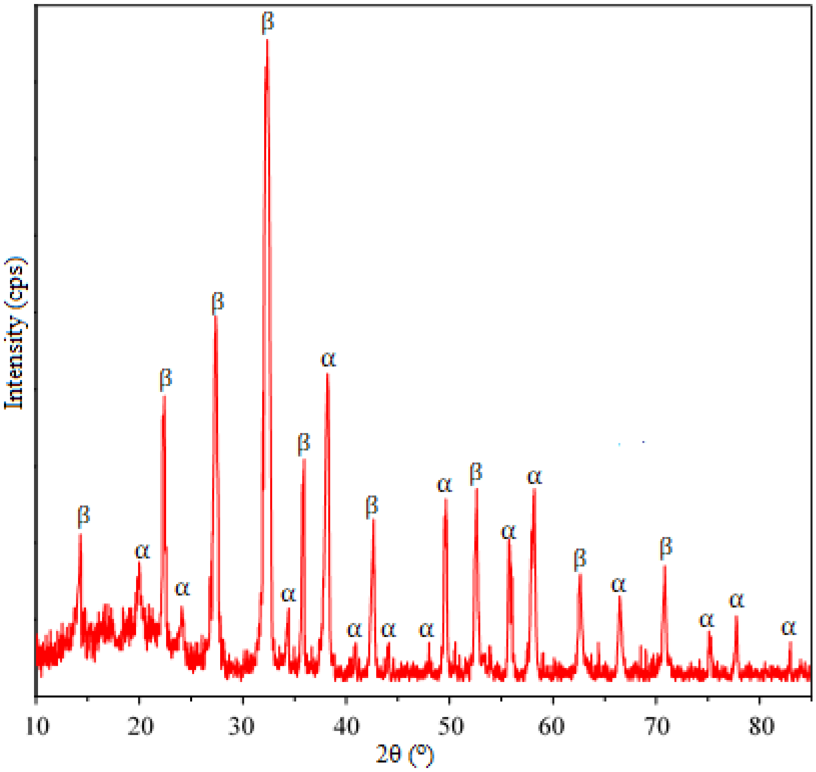

**Figure 8:** XRD spectrum of $Si_3N_4$ adsorbent

The XRD diffractogram (Figure 8) showed that $Si_3N_4$ adsorbent was the main phase dominated by α-$Si_3N_4$ as major phase (JCPDS-ICDD file No. 41-0360) and β- $Si_3N_4$ (JCPDS-ICDD file No. 33-1160) as minor phase. The profile Rietveld analysis showed the relative amount of α-$Si_3N_4$ and β-$Si_3N_4$ phases in the $Si_3N_4$ composite was 68.97 % and 31.03 % respectively. The high yield content of α-$Si_3N_4$ phase could be due to the use of high purity amorphous raw materials for carbothermal reduction and nitridation at low temperatures (Ji *et al.*, 2014). The broad peak patterns in all the XRD spectra signified that the $Si_3N_4$ was predominantly amorphous (Biesuz *et al.*, 2019).

### 3.3.3 SEM analysis

The SEM micrographs for $Si_3N_4$ adsorbent before and after adsorption was obtained at an accelerating voltage (20.0 kV) and magnification (Mg = 6.50 K X). The results are presented in Figure 9.

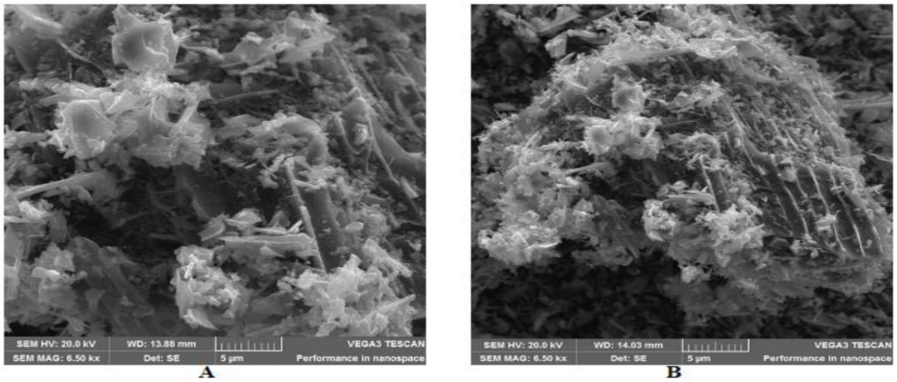

**Figure 9:** The SEM micrographs before (A) and after (B) adsorption

The results in Figure 9 showed the presence of rod-like and fiber-like micrographs. These are attributed to α-$Si_3N_4$ and β- $Si_3N_4$ structures (Ji *et al.*, 2014; Mahmut *et al.*, 2020). Before adsorption (A), the adsorbent surface evidenced pores of different shapes and sizes. The dye-loaded adsorbent surface (B) is more rigid and restrained which is contributed to dyes having occupied the pores.

### 3.3.4 EDX analysis

The elemental composition of $Si_3N_4$ adsorbent was determined using Energy Dispersive X-Ray (EDX) spectrometer. The spectrum is shown in Figure 10.

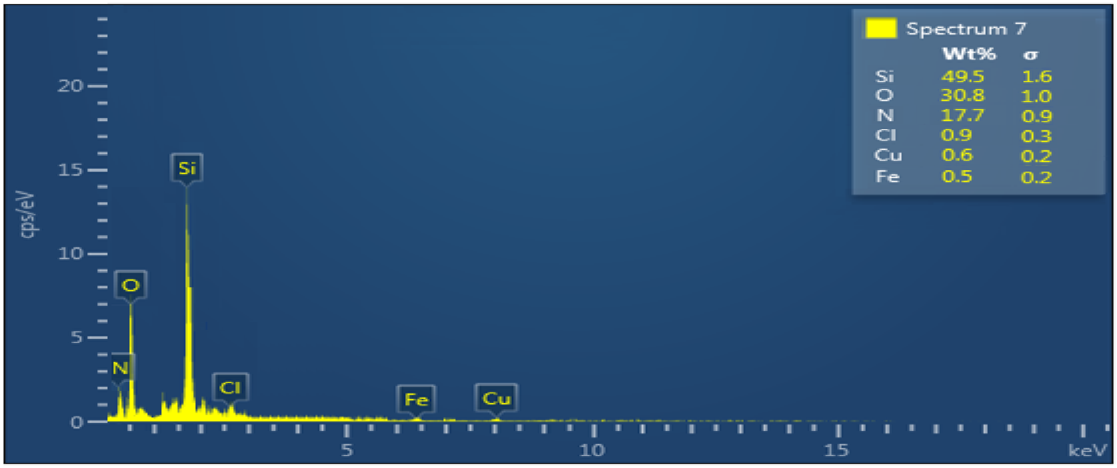

**Figure 10:** EDX spectrum of $Si_3N_4$

The results from EDX analysis showed that the elemental percentage composition of $Si_3N_4$ adsorbent was 49.5 % and 17.7 % for silicon and nitrogen respectively. Minor peaks for copper observed could be due to contamination from the copper grid sample holder (Huang *et al.*, 2013). The oxygen content could be due to the silica residues and minor metal oxide components (Abdulhameed *et al.*, 2018) of biochar samples after acid leaching and/or $Si_3N_4$ surface oxidation during the analysis (Qadri *et al.*, 2016). The chloride contents were detected in the $Si_3N_4$ powder. This could be due to residue acid (Bariş, 2014) from the biochar samples used for synthesis of $Si_3N_4$.

### 3.3.5 TGA analysis

The Thermogravimetric analysis of $Si_3N_4$ adsorbent was obtained at a varied temperature (0 °C - 600 °C), nitrogen gas flow rate (50 mL/min) and heating rate (15 °C/min). The TG curve is presented in Figure 11.

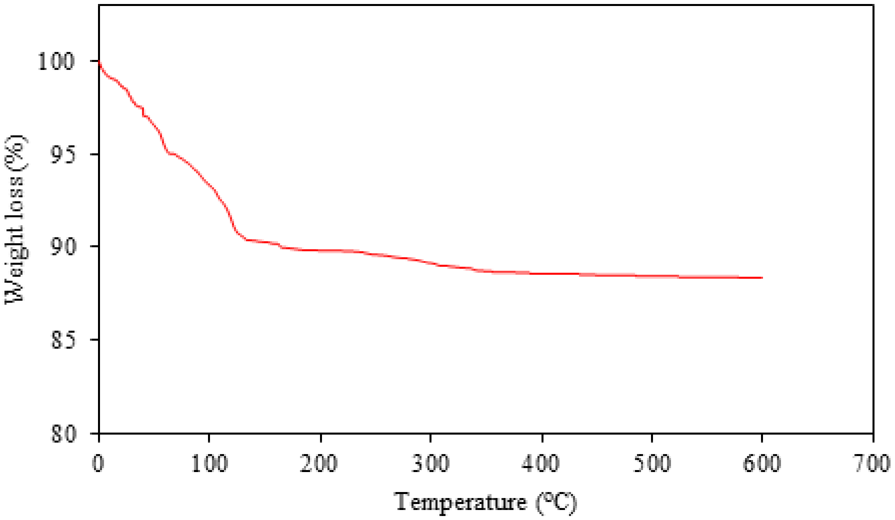

**Figure 11:** TG curve for $Si_3N_4$ adsorbent

The TGA curve for $Si_3N_4$ adsorbent represents two weight change steps. At the first step from 0 °C to around 150 °C with a weight loss of 9.63 % beyond which no thermal effect is detected and the weight change is already achieved. This could be attributed to the vaporization of adsorbed water molecules onto the $Si_3N_4$ surfaces after which it remains stable (Qiu *et al.*, 2019). The mass profile was then flat until 600 °C implying that the $Si_3N_4$ material is thermally stable even at high temperatures.

## 3.2 Fixed-bed column optimization

### 3.2.1 Effect of volumetric flow rate

The effect of volumetric flow rate on the MB dyes sorption onto $Si_3N_4$ adsorbent is shown in Figure 12.

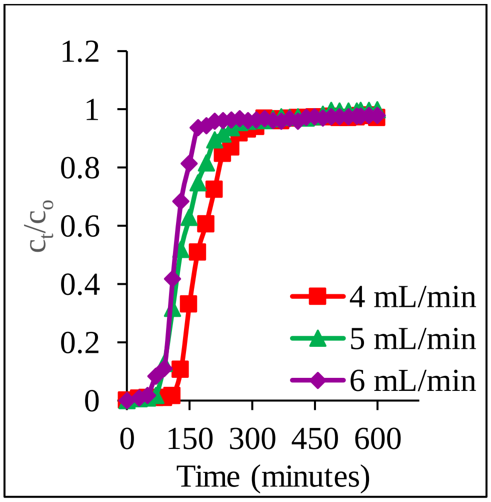

**Figure 12:** Effect of volumetric flow rate on sorption of MB dyes onto $Si_3N_4$ adsorbent (at $C_0$ = 50 mg/L, Z= 3 cm)

The column capacity of MB dyes sorption onto $Si_3N_4$ adsorbent was maximum at 4 mL/min. The breakthrough time ($t_b$) and saturation time ($t_s$) decreased with increase in flow rate. That is, 140 minutes to 70 minutes and 330 minutes to 200 minutes. This resulted to a decrease in column adsorption capacity to 42.24 ± 0.17 mg/g. This could be due to the fact that, at higher flow rate, the contact time of the dye molecules with the adsorbent surface is limited (Patel, 2018). This makes the molecules have inadequate time for their interaction with the adsorbent sites leaving the column before saturation occurs (Banerjee *et al.*, 2017; Hummadi *et al.*, 2022).

### 3.2.2 Effect of bed height

The breakthrough curves for column sorption of MB dyes were obtained at varied column bed heights of 3 cm, 5 cm and 7 cm. The results are presented in Figure 13.

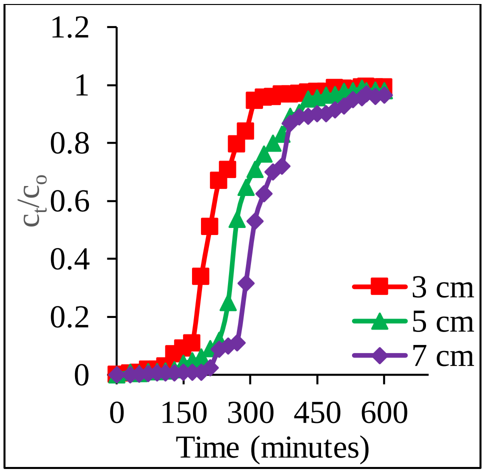

**Figure 13:** Effect of bed height on sorption of MB dyes onto $Si_3N_4$ adsorbent (at $C_0 = 50$ mg/L, Q= 4 mL/min)

The results (Figure 13) showed a maximum column capacity at optimal bed height of 7 cm. The breakthrough times ($t_b$), saturation times ($t_s$) and column adsorption capacity increased from 130 minutes to 210 minutes; 320 minutes to 550 minutes and 45.79 ± 0.04 mg/g to 48.75 ± 0.06 mg/g with increasing bed height (3 cm to 7 cm). At a bed height of 3, the adsorbent load is low, thus a smaller bed capacity, which over time becomes saturated and as a result, the dye concentration in the effluent solution is increased (Jain *et al.*, 2020). As the bed height is increases from 3 to 7 cm, a decrease in the slope of breakthrough curve is observed. This resulted to a rapid mass transfer zone (Jaime *et al.*, 2018). This was owed to the large adsorbents surface area leading to more binding sites for MB dyes sorption (Yahuza *et al.*, 2017).

### 3.2.3 Effect of influent concentration

The effect of influent concentration for the removal of MB dyes onto the adsorbent is shown in Figure 14.

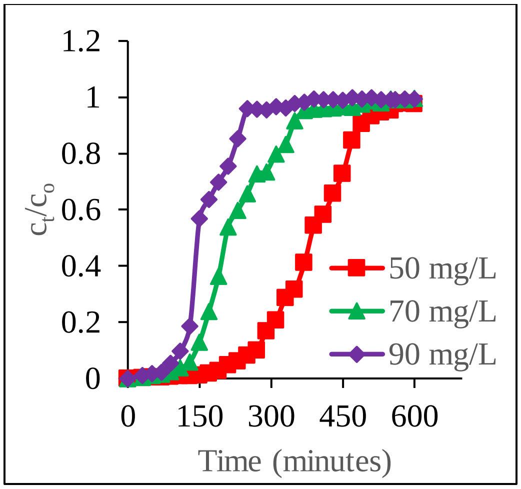

**Figure 14:** Effect of influent concentration on adsorption of MB dyes onto $Si_3N_4$ adsorbent (at Z = 7 cm, Q= 4 mL/min)

The maximum column capacity at optimal influent concentration (50 mg/L) was 47.01 ± 0.14 mg/g. Low initial dye concentration makes the saturation time of diffusion rate longer (Ali and Mohammed, 2021). The breakthrough curves became dispersed and breakthrough occurred slowly but sharper breakthrough curves were obtained as the influent concentration was increased (Al-Husseiny, 2014). This showed that, at lower inlet concentration, more dye molecules interact with the adsorbent sites leading to higher volume of treated water (Mohammad *et al.*, 2016). Increasing the influent concentration lead to a faster saturation of the active adsorbent sites lowering the dyes uptake (Hummadi *et al.*, 2022).

### 3.3 Column modelling

The kinetic plots of Yoon-Nelson, Thomas and Adam-Bohart were used to calculate the model parameters and constants. The results are presented in Table 3.

**Table 3:** Yoon-Nelson, Thomas and Adam-Bohart parameters

| **Thomas** | | | | | **Yoon-Nelson** | | | | | **Adams-Bohart** |
|---|---|---|---|---|---|---|---|---|---|---|
| **$Q_{o,\ exp}$ ± S.D (mg/g)** | **$Q_{o,\ cal}$ ± S.D (mg/g)** | **$K_{TH}$ (ml/mg/min)** | **$R^2$** | **$K_{YN}$ ($min^{-1}$)** | **$t_{0.5,\ exp}$ (min)** | **$\tau_{0.5,\ cal}$ (min)** | **$R^2$** | **$K_{AB}$ (L/mg/min)** | **$N_o$ (mg/L)** | **$R^2$** |
| 47.01 | 48.09 | $2.46 \times 10^{-4}$ | 0.996 | $2.14 \times 10^{-2}$ | 290 | 294.25 | 0.960 | $2.32 \times 10^{-4}$ | 3013.53 | 0.730 |

The results are consistent with both Thomas and Yoon-Nelson models as appropriate models to describe fixed-bed column operations ($R^2 > 0.919$). This indicates that column sorption mechanism of MB dyes onto the $Si_3N_4$ adsorbent was a monolayer chemical adsorption process (Zhang *et al.*, 2011). Also, the $\tau_{0.5,\ cal}$ value is comparable to the one obtained experimentally.

### 3.4 Column performance using spiked water samples

The column performance using spiked water samples was done at optimized parameters for $Si_3N_4$ adsorbent. The breakthrough curve obtained is presented in Figure 15.

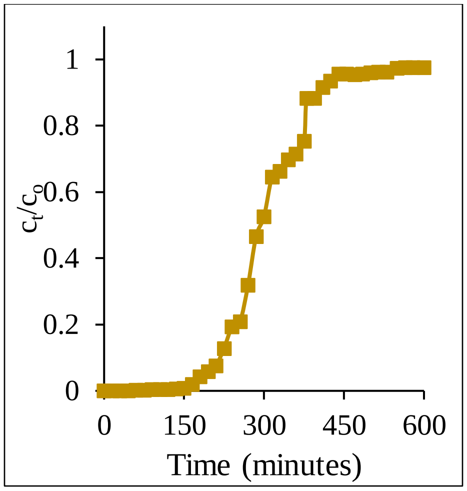

**Figure 15:** Column adsorption of MB dyes from spiked water samples onto $Si_3N_4$ adsorbent (at Q= 4 mL/min, Z = 7 cm)

The results in Figure 15 showed that the breakthrough and saturation times for $Si_3N_4$ adsorbent was 195 minutes and 440 minutes. The amount of dyes adsorbed ($Q_{o, exp}$) at saturation time was 38.92 ± 0.04 mg/g. The results showed that the adsorbent took less time to breakthrough and saturation for the spiked water samples than the model solutions with a lower column adsorption capacity. This could be due to the presence of other interfering organic and inorganic species in the water samples which competed for the available adsorbent sites with the dye molecules resulting to faster saturation of the adsorbent (Mahmoud *et al.*, 2019).

## 4. CONCLUSIONS

The study prepared $Si_3N_4$ powder using silica extracted from Bamburi Beach sand (BBS) and biochar from coffee husk wastes in an ammonia environment. The XRD, XRF and FT-IR results showed that quartz ($SiO_2$), calcite ($CaCO_3$), clinochlore ($((Mg, Fe)_6(Si, Al)_4O_{10}(OH)_8)$) and microcline (K (Al, Fe) $Si_3O_8$) as the main components of Bamburi Beach sand (BBS). The extracted silica contained silica as the main component (> 92 %), highly amorphous with hydroxyl (-OH) in silanol and siloxane (Si-O-Si) as important functional groups. The biochar samples obtained contained a porous carbon structure with aromatic carbon bonds (C=C) and a negligible ash content. The characterization of $Si_3N_4$ showed a porous composite with $\alpha$-$Si_3N_4$ phase and $\beta$-$Si_3N_4$ phases. The material was thermally stable at varied temperatures with important functional groups of Silicon-Nitrogen-Silicon (Si-N-Si), silanol (Si-OH) and Silicon-Nitrogen (Si-N) which were hydroxylated in an aqueous media to give silazane ($Si_2{=}NH_2^+$) and silanolate ($Si{-}O^-$) adsorbent sites for methylene blue (MB) dyes removal. Maximum dye uptake was obtained as 47.01 mg/g at optimal values of 4 mL/min, 7 cm and 50 mg/L. The breakthrough data were well fitted to Thomas and Yoon-Nelson models explaining a chemisorption process. The column performance for $Si_3N_4$ adsorbent using spiked water samples from river Athi gave a column capacity of 38.92 ± 0.04 mg/g.

## Acknowledgement

The authors are grateful to Kenyatta University for laboratory space, chemicals, reagents, equipments, instruments and technical support.

## Conflict of interest

The authors have disclosed no potential conflicts of interest

## 5. REFERENCES

Abdelhak, M., Ahmed, K., Abdelkader, B., Brahim, Z. and Rachid, K. (2014). Algerian Sahara sand dunes characterization. *Silicon*, 6: 149-154.

Abdulhameed, A., Mbuvi, H., Changamu, E. and Maingi, F. (2018). Synthesis of silicon nitride from rice husk and sugarcane bagasse ashes. *Journal of Water technology and Treatment methods*, 1 (1): 106-111.

Alghamdi, W. and El Mannoubi, I. (2021). Investigation of seeds and peels of *Citrullus colocynthis* as efficient natural adsorbent for methylene blue dye. *Processes*, 9 (8): 1279-1297.

Al-Husseiny, H.A. (2014). Adsorption of methylene blue dye using low cost adsorbent of sawdust: batch and continues studies. *Journal of Babylon University/Engineering Sciences*, 22 (2): 296-310.

Ali, H. and Mohammed, A. (2021). Removal of congo red from aqueous solution by circulating fluidized bed (CFB). *Association of Arab Universities Journal of Engineering Sciences*, 28 (2):1-7.

Alvarez, J., Lopez, G., Amutio, M., Bilbao, J. and Olazar, M. (2016). Preparation of adsorbents from sewage sludge pyrolytic char by carbon dioxide activation. *Process Safety and Environmental Protection*, 103: 76-86.

Alyosef, H., Ibrahim, S., Welscher, J., Inayat, A., Eilert, A., Denecke, R., Schwieger, W., Münster, T., Kloess, G., Einicke, W. Enke, D. (2014). Effect of acid treatment on the chemical composition and the structure of Egyptian diatomite. *International Journal of Mineral Processing*, 132: 17-25.

Aroke, U., Momoh, R., Hamidu, L. and Buhari, U. (2020). Removal of azo dye methyl orange in aqueous solution by kaolinite clay: Equilibrium isotherms, kinetics and error analyses. *Saudi Journal of Engineering and Technology*, 5 (11): 422-433.

Arunmetha, S., Karthik, A., Srither, R., Vinoth, M., Suriyaprabha, R., Manivasakan, P. and Rajendran, V. (2015). Size-dependent physicochemical properties of mesoporous nanosilica produced from natural quartz sand using three different methods. *RSC Advances*, 5 (59): 47390-47397.

Banerjee, S., Debsarkar, A. and Datta, S. (2017). Removal of basic dyes from aqueous solution by adsorption using rice husk ash-a fixed bed column study. *International Journal of Advanced Engineering, Management and Science*, 3 (4): 325-330.

Bariş, Y. (2014). Investigations of the productions of silicon nitride from Turkish rice husk. Thesis. The graduate school of natural and applied science, *Middle East University*.

Beddiaf, S., Chihi, S. and Leghrieb, Y. (2015). The determination of some crystallographic parameters of quartz, in the sand dunes of Ouargla, Algeria. *Journal of African Earth Sciences*, 106: 129-133.

Bennani, K.A., Mounir, B., Hachkar, M., Bakasse, M. and Yaacoubi, A. (2015). Adsorption of cationic dyes onto Moroccan clay: Application for industrial wastewater treatment. *Journal of Material and Environmental Science*, 6 (9): 2483-2500.

Biesuz, M., Bettotti, P., Signorini, S., Bortolotti, M., Campostrini, R., Bahri, M., Ersen, O., Speranza, G., Lale, A., Bernard, S. and Sorarù, G. D. (2019). First synthesis of silicon nanoscrystals in amorphous silicon nitride from a preceramic polymer. *Nanotechnology*, 30 (25): 255601-255620.

Bousbih, R., Haddadi, I., Zina, H., Alatawi, N. and Ezzaouia, H. (2020). Purification of Tabuk silica using chemical attack and thermal treatment. *Journal of Non-Oxide Glasses*, 12 (3): 27-30.

Bulgariu, L., Escudero, L. Bello, O., Iqbal, M., Nisar, J., Adegoke, K.A., Alakhras, F., Kornaros, M. and Anastopoulos, I. (2019). The utilization of leaf-based adsorbents for dyes removal: A review. *Journal of Molecular Liquids*, 276: 728-747.

Bushra, B. and Remya, N. (2020). Biochar from pyrolysis of rice husk biomass—characteristics, modification and environmental application. *Biomass Conversion and Biorefinery*, 10: 1-12.

Chang, R., Sohi, S.P., Jing, F., Liu, Y. and Chen, J. (2019). A comparative study on biochar properties and Cd adsorption behavior under effects of ageing processes of leaching, acidification and oxidation. *Environmental Pollution*, 254: 1-12.

Chen, C., Sun, K., Huang, C., Yang, M., Fan, M., Wang, A., Zhang, G., Li, B., Jiang, J., Xu, W. and Liu, J. (2023). Investigation on the mechanism of structural reconstruction of biochars derived from lignin and cellulose during graphitization under high temperature. *Biochar*, 5 (1): 51-64.

Cui, J., Li, B., Zou, C., Zhang, C. and Wang, S. (2015). Direct synthesis of α-silicon nitride nanowires from silicon monoxide on alumina. *Nanomaterials and Nanotechnology*, 5: 32-37.

El-Sawy, A., Gemeay, A.H., Helal, A.S. and Salem, M.A. (2021). Catalytic degradation of methylene blue in aqueous solution by $H_2O_2$ and $SiO_2$-$NH_2$-Cu(II)@$SiO_2$ nanoparticles as catalyst. *Journal of Molecular Liquids*, 341: 1-15.

Fachini, J., de Figueiredo, C., Joaquim, J., Rosa, S., da Silva, J. and do Vale, A. (2021). Novel K-enriched organomineral fertilizer from sewage sludge-biochar: Chemical, physical and mineralogical characterization. *Waste Management*, 135: 98-108.

Hachem, R., Meftah, N. and Bouaziz, A. (2023). A comparative analysis of the microstructural and physicochemical properties of alluvial and dune sands from northeast Algerian Sahara. *The Journal of Engineering and Exact Sciences*, 9 (6): 1-14.

Huang, J., Huang, Z., Yi, S., Liu, Y., Fang, M. and Zhang, S. (2013). Fe-catalyzed growth of one-dimensional α-$Si_3N_4$ nanostructures and their cathodoluminescence properties. *Scientific reports*, 3 (1): 1-9.

Huljana, M., Rodiah, S., Al Jabbar, J., Ichsan, C. and Marzuki, H. (2021). Silica-rice husk as adsorbent of Cr (VI) ions prepared through sol-gel method. *Walisongo Journal of Chemistry*, 4 (1): 65-73.

Hummadi, K., Luo, S. and He, S. (2022). Adsorption of methylene blue dye from the aqueous solution *via* bio-adsorption in the inverse fluidized-bed adsorption column using the torrefied rice husk. *Chemosphere*, 287: 1-11.

Iheanacho, O.C., Nwabanne, J., Obi, C., and Onu, C.E. (2021). Packed bed column adsorption of phenol onto corn cob activated carbon: Linear and nonlinear kinetics modeling. *South African Journal of Chemical Engineering*, 36: 80-93.

Jagdale, P., Ziegler, D., Rovere, M., Tulliani, J.M. and Alberto, T. (2019). Waste coffee ground biochar: A material for humidity sensors. *Sensors,* 19 (4): 801-816.

Jaime, L., Dalia, I., Reyna, G. and Ma, A. (2018). Study of a fixed-bed column in the adsorption of an azo dye from an aqueous medium using a chitosan–glutaraldehyde biosorbent. *Adsorption Science & Technology,* 36 (1-2): 215-232.

Jain, S., Tamboli, S.R., Sutar, D.S., Jadhav, S., Marathe, J., Shaikh, A. and Prajapati, A. (2020). Batch and continuous studies for adsorption of anionic dye onto waste tea residue: Kinetic, equilibrium, breakthrough and reusability studies. *Journal of Cleaner Production*, 252: 1-35.

Jhansirani, K., Dubey, R., More, M. and Singh, S. (2016). Deposition of silicon nitride films using chemical vapor deposition for photovoltaic applications. *Results in Physics,* 6, 1059-1063.

Ji, H., Huang, Z., Chen, K., Li, W., Gao, Y., Fang, M., Liu, Y. and Wu, X. (2014). Synthesis of $Si_3N_4$ powder with tunable α/β-Si3N4 content from waste silica fume using carbothermal reduction nitridation. Powder Technology, 252: 51-55.

Kabayo, S., Kindala, J., Nkanga, C., Krause, R. and Taba, K. (2019). Preparation and characterization of solid acid catalysts derived from coffee husks. *International Journal of Chemical Science*, 3 (6): 5-13.

Kobayashi, S. (2016). IR spectroscopic study of silicon nitride films grown at a low substrate temperature using very high frequency plasma-enhanced chemical vapor deposition. *World Journal of Condensed Matter Physics*, 6, 287-293.

Krishna Murthy, T., Gowrishankar, S., Krishna, R. H., Chandraprabha, M. and Mathew, B. (2020). Magnetic modification of coffee husk hydrochar for adsorptive removal of methylene blue: isotherms, kinetics and thermodynamic studies. *Environmental Chemistry and Ecotoxicology,* 2: 205-212.

Lawrinenko, M. and Laird, D.A. (2015). Anion exchange capacity of biochar. *Green Chemistry,* 17 (9): 4628-4636.

Liang, G., Sun, G., Bi, J., Wang, W., Yang, X. and Li, Y. (2020). Mechanical and dielectric properties of functionalized boron nitride nanosheets/silicon nitride composites. *Ceramics International*, 47 (2), 2058-2067.

Liu, Q., Zhou, Y., Wang, M., Zhang, Q., Ji, T., Chen, T. and Yu, D. (2019). Adsorption of methylene blue from aqueous solution onto viscose-based activated carbon fiber felts: Kinetics and equilibrium studies. *Adsorption Science & Technology*, 37 (3): 1-21.

Mahmoud, M., Nabil, G., Khalifa, M., El-Mallah, N. and Hassouba, H. (2019). Effective removal of crystal violet and methylene blue dyes from water by surface functionalized zirconium silicate nanocomposite. *Journal of Environmental Chemical Engineering*, 7 (2): 1-17.

Mahmut, S., Mustafa, G., Ali, Ç. and Gülsüm, T. (2020). Silicon nitride ceramic for all-ceramic dental restorations. *Dental Materials Journal*, 39 (6): 1080-1086.

Mansuri, I., Farzana, R., Rajarao, R. and Sahajwalla, V. (2018). Carbon dissolution using waste biomass—A sustainable approach for iron-carbon alloy production. *Metals*, 8 (4): 290-301.

Maroufi, S., Mayyas, M., Nekouei, R., Assefi, M. and Sahajwalla, V. (2018). Thermal nanowiring of e-waste: A Sustainable route for synthesizing green $Si_3N_4$ nanowires. *ACS Sustainable Chemistry & Engineering*, 6 (3): 3765-3772.

Mcyotto, F., Wei, Q., Macharia, D.K, Huang, M., Shen, C. and Chow, C. (2021). Effect of dye structure on color removal efficiency by coagulation. *Chemical Engineering Journal*, 405: 1-13.

Meftah, N. and Mahboub, M. (2019). Spectroscopic Characterizations of sand dunes minerals of El-Oued (Northeast Algerian Sahara) by FTIR, XRF and XRD analyses. *Silicon*, 12 (1): 147-153.

Meftah, N., Hani, A. and Merdas, A. (2023). Extraction and physicochemical characterization of highly-pure amorphous silica nanoparticles from locally available dunes sand. *Chemistry Africa*, 6, 1-10.

Mohammad, F., Mohamad, E., Hossein, A., Alireza, S. and Ehsan, S.P. (2016). Continuous adsorption study of congo red using tea waste in a fixed-bed column. *Desalination and Water Treatment*, 57 (18): 8437-8446.

Mu, B., Wang, H., Hao, X. and Wang, Q. (2018). Morphology, mechanical properties and dimensional stability of biomass particles/high density polyethylene composites: Effect of species and composition. *Polymers*, 10 (3): 308-322.

Muliwa, A.M., Mecha, A.C., Grobler, A. and Onyango, M.S. (2016). Removal of multi-active blue dye from aqueous phase using magnetic poly-pyrrole nanocomposites: Fixed-bed adsorption studies. *Research Journal of Applied Sciences, Engineering and Technology*, 13 (7): 576-584.

Munasir, Sulton, A., Triwikantoro, Zainuri, M. and Darminto. (2013). Synthesis of silica nanopowder produced from Indonesian natural sand via alkali fusion route. *American Institute of Physics*, 1555 (1): 28-31.

Munasir, Triwikantoro, Zainuri, M. and Darminto, (2015). Synthesis of $SiO_2$ nanopowders containing quartz and cristobalite phases from silica sands. *Materials Science-Poland*, 33 (1): 47-55.

Ndung'u S.N, Wanjau, R. and Nthiga, E. (2022). Fixed bed column studies of selected phenols and dyes using low-cost adsorbents. *Asian Journal of Research in Chemistry*, 15 (3): 189-194.

Ndung'u S.N., Nyahanga T., Wanjau Ruth N. and Nthiga Esther W. (2021). Adsorption evaluation of selected heavy metal ions by amino-functionalized low-cost adsorbents. A Review. *Global Scientific Journals*, 9 (7): 339-357.

Ndung'u, S., Nthiga, E., Wanjau, R. and Ndiritu, J. (2021). Adsorption studies of lead (II) ions from a synthetic media using Jackfruit (*Artocarpus heterophyllus L.)* rags: Kinetics, equilibrium and thermodynamic studies. *International Journal of Scientific Research in Chemical Sciences*, 8 (4): 5-12.

Ndung'u, S.N., Nthiga, E.W. and Wanjau, R.N. (2023 b). Characterization of amorphous silicon nitride prepared from sand and coffee husk wastes by carbothermal reduction-nitridation. *African Journal of Pure and Applied Sciences*, 4 (3): 24-34.

Ndung'u, S.N., Wanjau, R.N. and Nthiga, E.W. (2024). Efficacy of adsorption of Congo Red dyes from an aqueous media using Silicon Nitride ($Si_3N_4$) adsorbent derived from sand and coffee husk wastes. *Eurasian Journal of Science and Technology*, 4 (3): 253-263.

Ndung'u, S.N., Wanjau, R.N. and Nthiga, E.W. (2023 a). Facile extraction and characterization of silica nanopowder from marine national park beach sand via alkali fusion route. *International Journal of Technology,* 13, (1): 1-6.

Ngulube, T., Gumbo, J., Masindi, V. and Maity, A. (2017). An update on synthetic dyes adsorption onto clay based minerals: A state-of-art. *Journal of Environmental Management*, 191: 35-57.

Nica, I., Biliuta, G., Zaharia, C., Rusu, L., Coseri, S. and Suteu, D. (2020). Fixed-bed column studies for methylene blue removal by cellulose cellets. *Environmental Engineering and Management Journal*, 19 (2): 269-279.

Nthiga, E., Ndung'u, S., Kibet, K. and Wanjau, R. (2021). Removal of $Cr^{3+}$ ions from a model solution by HCl treated *Artocarpus heterophyllus* L. seeds: Equilibrium and kinetic study. *International Journal of Research and Innovation in Applied Science,* 6 (2), 38-45.

Panwar, K., Jassal, M. and Agrawal, A. (2015). In situ synthesis of Ag-$SiO_2$ anus particles with epoxy functionality for textile applications. *Particuology*, 19: 107-112.

Parmar, N. and Shukla, S. (2019). Decolourization of dye wastewater by microbial methods-A review. *Indian Journal of Chemical Technology,* 25 (4): 315-323.

Patel, H. (2018). Adsorptive batch and column studies of Congo Red onto gulmohar leaf powder. *European Journal of Chemistry*, 9 (2): 107-114.

Patel, H., Vashi, R. and Champaneri, V. (2019). Continuous adsorption of methylene blue dye from aqueous solution onto guava leaf powder in fixed bed. *Journal of Applicable Chemistry*, 8 (5): 2246-2254.

Qadri, S., Rath, B., Gorzkowski, E., Wollmershauser, J. and Feng, C. (2016). Nanostructured silicon nitride from wheat and rice husks. *Journal of Applied Physics*, 119 (13): 1-7.

Qiu, B., Li, M., Xu, B., Liu, P., Chen, Q., Xu, B. and Han, Z. (2019). Effects of amino groups on dispersibility of silicon nitride powder in aqueous media. *Ceramics International*, 45 (4), 4268-4273.

Ramdani, N., Wang, J., Wang, H., Feng, T., Derradji, M. and Liu, W. (2014). Mechanical and thermal properties of silicon nitride reinforced polybenzoxazine nanocomposites. *Composites Science and Technology*, 105: 73-79.

Saha, P., Chowdhury, S., Mondal, M. and Sinha, K. (2012). Biosorption of direct red 28 (congo red) from aqueous solutions by eggshells: Batch and column studies. *Separation Science and Technology*, 47: 112-123.

Sahoo, K., Kumar, A. and Chakraborty, J.P. (2020). A comparative study on valuable products: bio-oil, biochar, non-condensable gases from pyrolysis of agricultural residues. *Journal of Material Cycles and Waste Management*, 23: 186-204.

Shi, C., Zhu, Y., Qian, H. and Lu, L. (2014). Fabrication of silicon nitride fiber–PMMA composite through free radical polymerization in batch. *Materials Research Bulletin*, 51: 161-166.

Yahuza, K., Ibrahim, M., Ayuba, A. and Hamza, R. (2017). Fixed-bed column adsorption of methyl blue using carbon derived from axle-wood (*Anogeissus leiocarpus*) stem as adsorbent. *Bayero Journal of Pure and Applied Sciences*, 10 (1): 304-310.

Yang, H., Mu, B., Zhang, T., Lu, Y. and Wang, A. (2023). Sustainable utilization of natural sands for cleaner preparation of high-performance nanostructured cobalt blue composite pigments by dolomite induced mechanochemistry. *RSC Sustainability*, 1: 1278-1289.

Yue, C., Liu, J., Zhang, H., Dai, L., Wei, B. and Chang, Q. (2018). Increasing the hydrophobicity of filter medium particles for oily water treatment using coupling agents. *Heliyon*, 4 (9): 1-14.

Zhang, W., Dong, L., Yan, H., Li, H., Jiang, Z., Kan, X., Yang, H., Li, A. Cheng, R. (2011). Removal of methylene blue from aqueous solutions by straw based adsorbent in a fixed-bed column. *Chemical Engineering Journal*, 173 (2): 429-436.

Zouaouid, K. and Gheriani, R. (2018). Mineralogical analysis of sand roses and sand dunes samples from two regions of South Algeria. *Silicon*, 11 (3): 1537-1545.